Sedimentology (2003) **50**, 279–301

Direct numerical simulation of bedload transport using a local, dynamic boundary condition

MARK W. SCHMEECKLE* and JONATHAN M. NELSON†
**Florida State University, Department of Geological Sciences, Center for Earth Surface Processes Research, 108 Carraway Building, Tallahassee, FL 32306, USA (E-mail: schmeeckle@fsu.edu)*
†United States Geological Survey, Water Resources Division, Denver Federal Center, MS-413, PO Box 25046, Lakewood, CO 80225, USA

ABSTRACT

Temporally and spatially averaged models of bedload transport are inadequate to describe the highly variable nature of particle motion at low transport stages. The primary sources of this variability are the resisting forces to downstream motion resulting from the geometrical relation (pocket friction angle) of a bed grain to the grains that it rests upon, variability of the near-bed turbulent velocity field and the local modification of this velocity field by upstream, protruding grains. A model of bedload transport is presented that captures these sources of variability by directly integrating the equations of motion of each particle of a simulated mixed grain-size sediment bed. Experimental data from the velocity field downstream and below the tops of upstream, protruding grains are presented. From these data, an empirical relation for the velocity modification resulting from upstream grains is provided to the bedload model. The temporal variability of near-bed turbulence is provided by a measured near-bed time series of velocity over a gravel bed. The distribution of pocket friction angles results as a consequence of directly calculating the initiation and cessation of motion of each particle as a result of the combination of fluid forcing and interaction with other particles. Calculations of bedload flux in a uniform boundary and simulated pocket friction angles agree favourably with previous studies.

Keywords Bedload, equations of motion, numerical simulation, sediment transport, turbulence.

INTRODUCTION

The formation and evolution of sedimentary bed features, such as scours, bedload sheets, ripples, dunes, bars, armour, sorting and grading, are ubiquitous in both fluvial and marine environments. These features in the geological record are primarily classified by their characteristic geometric forms and size sorting. In nearly all cases, both form and sorting are produced by a spatially and temporally varying sediment transport field resulting from interaction of a turbulent flow with the sediment grains of an erodible bed. Although sedimentologists have been able to discern the conditions under which these features were formed by comparison with modern environmental analogues, a number remain to be explained in a physical, quantitative manner.

The lack of accurate physical models of a number of sedimentary structures produced by bedload transport can be explained by the fact that the motion of mixed grain-size sediment, by rolling and saltation along the bed of a turbulent flow, is an inherently complex problem. Turbulence produces fluctuations in the near-bed velocity that give rise to fluctuations in the forces on, and resultant motion of, sediment grains. Some particles near the bed surface are surrounded by particles much higher in the flow, whereas others protrude above adjacent grains and therefore experience greater drag forces from the flow. The geometric arrangement of surrounding grains also leads to variability of forces required to begin motion. In other words, particles that rest in deep bed pockets are harder to move than particles in shallow pockets. Previous attempts at modelling bedload sediment motion have spatially and temporally averaged most or all of these sources of variability that make the problem difficult.

The flux of bedload sediment in open channel flows is generally calculated as a monotonic function of the near-bed fluid shear stress. This boundary shear stress is a time-averaged quantity, and the near-bed fluid shear stress must equal the force of the flow on the bed particles. Hence, a greater force on the particles should lead to a proportionate increase in the downstream flux of sediment. However, this equality of the force per unit area of the bed particles on the fluid and the momentum flux in the near-bed fluid does not hold instantaneously. At a given instant, the vertical transport of momentum in the fluid is not necessarily correlated with forces on the sediment bed. Stresses in a turbulent fluid are actually 'apparent' or Reynolds stresses, which result from time-averaging of the spatial acceleration terms of the Navier–Stokes equations. The downstream Reynolds shear stress from vertical transport of momentum is $-\rho_f \overline{u'_x u'_z}$, where ρ_f is the fluid density, u'_x and u'_z are the instantaneous downstream and vertical velocity fluctuations, respectively, and the overbar represents a time average. Instantaneously, the near-bed fluid is accelerating, and the force of the fluid on the sediment bed is not equal to the Reynolds stress in the fluid. For example, consider a situation in which u'_x and u'_z are positive (i.e. flow is away from the bed, and the downstream velocity is greater than average). The downstream drag on a particle will be greater than average, and the flow away from the bed will help to offset the weight of the particle, but $-\rho_f u'_x u'_z$ is opposite in sign to the Reynolds stress. Thus, the instantaneous value, $-\rho_f u'_x u'_z$, is of little use in predicting the instantaneous force on particles in the sediment bed and, therefore, of little use in predicting instantaneous entrainment of bed particles.

If the frequency and magnitude of the near-bed velocity fluctuations were to scale with the boundary shear stress, then it could be argued that the boundary shear stress characterizes the mean and fluctuating forces on bedload particles. However, the magnitude of turbulent velocity fluctuations, $\overline{u'^2}$, scales with u_* only when there is a constant roughness length and density of particles on the bed (Bayazit, 1975; Nowell & Church, 1979). Furthermore, and perhaps more critically, the velocity fluctuations scale with the shear velocity only when the flow is uniform. The fact that velocity fluctuations scale with the shear velocity in a turbulent boundary layer has led to the successful application of similarity relationships for quantities such as $\overline{u'^2_x}/u^2_*$ and $\overline{u'^2_z}/u^2_*$ being only functions of relative height within a boundary layer (e.g. Stull, 1988). These similarity relationships break down in non-uniform flow because the turbulence structure at a particular point in the flow is largely inherited from upstream. In a specific example, McLean *et al.* (1994) and Nelson *et al.* (1993) have shown that the ratio of the magnitude of turbulent fluctuations to the shear stress on the stoss of a bedform is considerably higher than that in a uniform boundary layer. They attributed this effect to low-frequency fluctuations produced in the free shear layer caused by flow separation at the dune crest. For other types of non-uniform flow, such as a change in roughness or a channel constriction, relatively little is known about the near-bed turbulent structure. A physical model of the coupling between sediment motion and turbulent velocity fluctuations of arbitrary frequency and magnitude is needed so that transport can be calculated in any non-uniform flow.

Physical models of bedload transport rely on the Bagnold (1956) or Owen (1964) boundary condition, which states that moving grains will extract enough momentum from the fluid in the bedload layer, such that the fluid stress at the bed remains at the critical shear stress. Ashida & Michiue (1972) were perhaps the first to apply this boundary condition successfully to obtain a semi-theoretical model of bedload sediment flux. The only empirical components of this model are the dynamic friction coefficient and the critical shear stress. The dynamic friction coefficient is the ratio of the downstream-directed stress to the normal stress of moving grains on the bed. The stress that opposes motion in the downstream direction is caused primarily by collision and rolling of moving particles with the bed, whereas the normal stress is produced by the gravitational force on the moving grains. Since the work of Ashida & Michiue (1972), considerable attention has been given to the forces on, and resultant motion of, representative individual grains with the idea that a semi-theoretical method for calculating the dynamic friction coefficient and critical shear stress could be derived. Using temporally and spatially averaged fluid velocities for uniform turbulent boundary layer flows, several researchers have formulated the particle equations of motion and simulated the trajectories of saltating particles (van Rijn, 1984; Wiberg & Smith, 1985; Sekine & Kikkawa, 1992; Lee & Hsu, 1994; Niño & Garcia, 1994). In this manner, the height, length and velocity of saltation trajectories are calculated and generally agree with direct measurements. However, Niño *et al.* (1994) and Niño & Garcia (1994) experimentally determined the dynamic friction coefficient by measuring saltation statistics and momentum exchange with the bed using video, and found that previous researchers had used dynamic friction coefficients that are too high. Niño & Garcia (1994) then used the measured friction coefficient with the Bagnold boundary condition to predict the bedload concentration of bedload particles and a model of bedload flux. The resulting model greatly overpredicts measurements of bedload flux; the concentration of particles required by the Bagnold condition is too large. To bring the bedload predictions in line with measurements of transport requires the use of dynamic friction coefficients far in excess of friction coefficients based on measurements.

Fernandez-Luque & van Beek (1976) measured saltation statistics such as hop length, particle velocity and momentum loss during impact while simultaneously measuring sediment flux. They calculated the reduction in fluid shear stress by moving grains based on these measurements and found that, when ratios of the boundary shear stress to the critical boundary shear stress, commonly called the transport stage, are less than about three, the amount of momentum extracted from the fluid by moving grains is much less than required by the Bagnold condition. The Bagnold boundary condition for bedload sediment transport below a transport stage of about three is apparently not correct. This result has direct implications for a large number of rivers. For example, all transport occurs at transport stages less than three in most gravel-bed streams.

The reason for the failure of the Bagnold condition at low transport stages may be because it averages the temporal and spatial variability of the near-bed turbulence. The most notable feature of bedload transport at low transport stages, when viewed using high-speed motion photography, is that transport is highly episodic (Grass, 1970; Nelson *et al.*, 1995; Gyr & Schmid, 1997). Movement of grains over a particular area of the bed occurs for a period of time followed by a period in which little or no motion occurs. Nelson *et al.* (1995) and Grass (1970) have shown that periods of significant motion correspond to instances in which the near-bed downstream velocity is high, with little correlation to the vertical velocity. At low transport stages, the mean near-bed velocity is capable of transporting little or no sediment, and almost all transport occurs when the near-bed downstream velocity is well above the mean. Therefore, a physically based model of sediment transport must account for the temporal and spatial variability of the near-bed fluid velocity. The Bagnold or Owen boundary condition works at higher transport stages, because the mean downstream velocity is capable of entraining grains. Hence, the concentration of entrained particles will increase until enough momentum is extracted by saltating grains to equalize the rates of entrainment and disentrainment of grains. In contrast, at low transport stages, entrainment is controlled by the temporal and spatial extent of turbulent events with high downstream velocity.

A modification of the Bagnold boundary condition at low transport stages should account for the temporal and spatial variability of near-bed turbulence. The approach taken here is to simulate the motion of a large number of grains numerically by integrating their equations of motion simultaneously. The downstream force on grains is dependent on the downstream flow around them. Thus, a model is developed in which each particle moves in response to the local and temporally variable velocity field. An assumption in this study is that the velocity field near a sediment grain can be broken into two separate pieces: the overlying turbulence and the modification of that turbulent velocity field by other upstream sediment grains. The temporal and spatial variability of turbulent velocities above a sediment bed can be measured using a number of velocimetry techniques, or it can perhaps be obtained by numerical simulations of turbulence. However, as grains move around during transport, they modify the velocity field at the vertical level of the fluid where some grains are present. Hence, the presence of sediment grains modifies the velocity field felt by downstream grains. Unfortunately, no data or model exists for how protruding bed particles modify the velocity incident on downstream grains. Accordingly, the first section of this paper reports on measurements of velocity downstream of protrusive bed particles in a laboratory flume. An empirical model of the velocity reduction by protruding particles is then used in the development of a model that directly simulates the motion of all the particles in a sediment bed.

A temporally and spatially variable overlying turbulence field combines with the local configuration of grains to produce a local, dynamic boundary condition that determines the motion of sediment grains.

VELOCITY STRUCTURE VERY NEAR THE SEDIMENT BOUNDARY

The results of experiments involving the direct, high-frequency measurement of forces on a fixed bed particle simultaneously with high-frequency measurement of velocity within a grain diameter of the particle reveal that the instantaneous downstream force is highly correlated with the instantaneous near-grain velocity (Schmeeckle, 1998). Sekine & Kikkawa (1984) studied videotapes of the geometry of a sediment bed during bedload transport and determined that the deviation of the centroid of a particle from the mean bed elevation of all the particles' centroids making up the top layer of the bed is approximately a Gaussian distribution. If this distribution is accurate, at three standard deviations above the mean, the centroid of a grain is one grain diameter above the mean elevation. Thus, it is very rare for a particle in a natural bed to protrude its entire area above the mean elevation, but this does not preclude the possibility that grains surrounding a grain well above the mean are not themselves above the mean; particle clusters of several to tens of grains that protrude above the mean bed elevation are a common feature, particularly of coarse-grained beds (Robert, 1990; Gomez, 1993). Therefore, almost every particle is partially in the wake of upstream particles, and particles smaller than the mean grain size are generally entirely below the level of upstream particles. It is therefore necessary to quantify the velocity reduction in the wakes of bed particles compared with the velocity above the bed. Both the mean velocity reduction in the wake of protruding particles and the variability of the velocity are important for entrainment. In the case of grains smaller than the mean diameter in mixed grain-size sediment, the smaller particles may have little, if any, incident mean downstream velocity and are entrained largely by velocity fluctuations.

Previous attempts to model this local reduction in velocity resulting from the presence of upstream grains, in the context of sediment transport or initial motion studies, have generally been accomplished by adjusting the height of the particle relative to the wall log velocity profile. Realizing that the log profile does not hold below the tops of bed grains, Wiberg & Smith (1987), using a method similar to that of Roberson & Chen (1970), calculated the drag on bed particles, subtracted this stress from the total stress to obtain a fluid stress and then integrated to get the velocity profile. Wiberg & Smith (1987) proposed that this velocity profile could be used to calculate forces on grains for initial motion studies of streams with high roughness to depth ratios. Kirchner *et al.* (1990) measured distributions of friction angles of bed pockets as well as distributions of the protrusion of the tops of grains above the mean bed elevation and distributions of the heights of particles relative to maximum bed elevation within a characteristic diameter upstream. These latter two measures of grain exposure imply that there is a broad distribution of the relative incident velocities on the upstream faces of bed particles even within a size class. Some grains see large incident velocities and others do not; there is a broad spatial distribution of forces on particles of a single grain size. Thus, for the direct calculation of entrainment, methods that assume a horizontally uniform reduction in velocity as a result of the drag on bed particles will fail to capture the spatial variability of the problem.

Here, a quantitative understanding of the velocity in the wake of a bed particle is sought so that, given a particular upstream geometry and a near-bed velocity above the tops of the grains, the incident velocity on the face of a grain can be calculated. The theory that exists on the velocity structure in turbulent wakes is not applicable to this problem. For example, Schlichting (1979) presented a similarity theory for the velocity in wakes, but the similarity does not hold until tens of particle diameters downstream; grains that comprise a bed are in contact with one another, and the wake area of interest is within several diameters downstream. Also, these semi-theoretical treatments were not formulated or tested for the case at hand in which there is shear and rough boundary layer turbulence. The aim of the experiments in this study is thus to approach the problem empirically by measuring the velocity field downstream and below the tops of particles protruding from an experimental bed. These results are then the basis for determining the force on individual particles in a direct numerical simulation of bedload transport.

Experiments

In order that the velocity at points downstream of, and below, the tops of bed particles could be measured, large, 0·075 m diameter, plastic spheres were placed on the bed of a racetrack water flume. Time series of velocity in the vertical and downstream direction were measured using a laser Doppler velocimeter (LDV) above and below the tops of these particles. The LDV measures the velocity of small particles that traverse the sample volume where the four laser beams cross and, thus, the velocity measurements are not equally spaced in time. A more complete description of the flume and LDV set-up can be found in Nelson *et al.* (1993). Each measurement of a velocity time series at a point ran for at least 30 s and comprised more than 1000 instantaneous velocity measurements (data rate = 5–150 Hz). A small hole was drilled in the spheres to fill them with sand and water. The width of the flume was adjusted to 0·38 m using a false wall so that five spheres could be lined up in the cross-stream direction. In all the experiments, the spheres were lined up in rows of five with the neighbouring rows touching one another. There were 50 rows, and the measurements were taken either between the 38th and 39th row downstream or above the 39th row. The depth of the flow was 0·245 ± 0·004 m measured from the water surface to the Plexiglas bed. Thus, the total depth of flow was only slightly greater than three particle diameters. At these shallow depth to roughness ratios, a true logarithmic wall layer turbulence is not expected to develop (Pitlick, 1992).

Two sets of experiments were conducted. In one set of experiments, the spheres were all at the same height resting on the bed, and a single wake ball was placed in the pocket formed by four balls between two rows. Placement of the wake ball in this position, resting on four balls, resulted in the top of the wake ball being 0·048 m above the tops of the bed spheres. Vertical profiles of velocity were made downstream of the wake sphere at the same cross-stream position as the centre of the wake particle. The horizontal position of the measurements remained the same, whereas the wake particle was moved to successive upstream pockets. A vertical profile was also made with the sphere removed from the flow so that the effect of the wake sphere on the velocity profile could be ascertained. In the second set of experiments, the bed was roughened by raising bed particles from the bed of the flume by placing pieces of wood under them. Four different roughness arrangements were formed: (1) every third sphere in the downstream direction was 0·023 m above the bed; (2) every fourth sphere downstream was 0·017 m above the bed; (3) every sixth downstream sphere was 0·023 m above the bed; and (4) every eighth particle was 0·017 m above the bed. In each case, the sequence was staggered such that all spheres in a given row were not raised. In these experiments, one of the balls was connected to a 0·006 m threaded, cylindrical rod on an aluminium base. The height of this wake ball could be adjusted to any position above the bed. The protrusion height of the wake ball was adjusted from 0·036 to 0·017 m above the tops of the bed particles. Measurements were taken downstream of this particle in a similar manner to that of the 'smooth'-bed experiments. Figure 1 is a photograph of the experimental set-up for the near-bed experiments illustrating the arrangement of spheres in case (1) above, where every third ball in the downstream direction is 0·023 m above the other spheres. The height-adjustable wake sphere is shown next to the laser probe.

RESULTS

The results of the smooth-bed case show a very sharp reduction in the mean downstream velocity, $\overline{U_{xr}}$, just downstream and below the top of the wake particle, compared with the velocity, $\overline{U_{xo}}$, at the same position when the wake particle is removed. Figure 2 shows the velocity profiles downstream of the wake particle for an experiment in which the discharge was held constant.

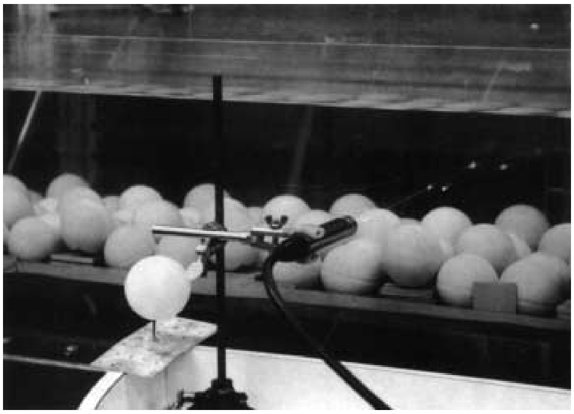

Fig. 1. Experimental set-up for the near-bed velocity experiments. Each sphere has a diameter of 0·075 m. The wake ball whose height could be adjusted is shown next to the fibre-optic laser probe. In the photograph, every third ball in the downstream direction is 0·023 m above the other spheres.

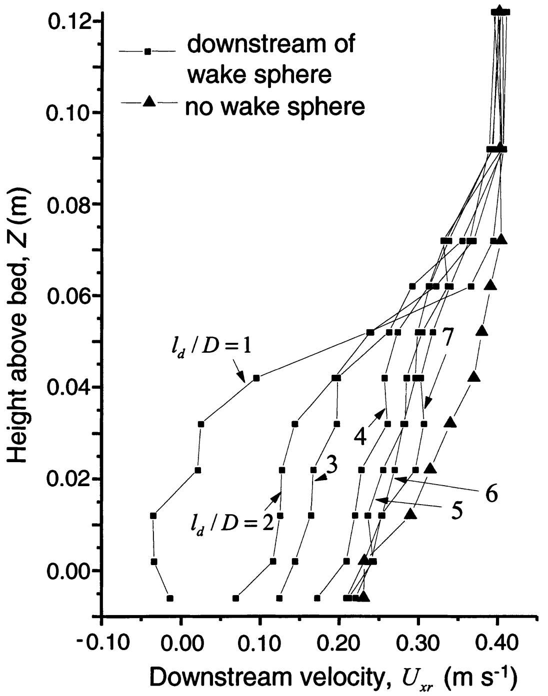

Fig. 2. Velocity profiles downstream of the wake sphere. Seven profiles of downstream distance, l_d, over the diameter of the spheres, D, are shown. The top of the wake sphere is at $Z = 0{\cdot}048$ m.

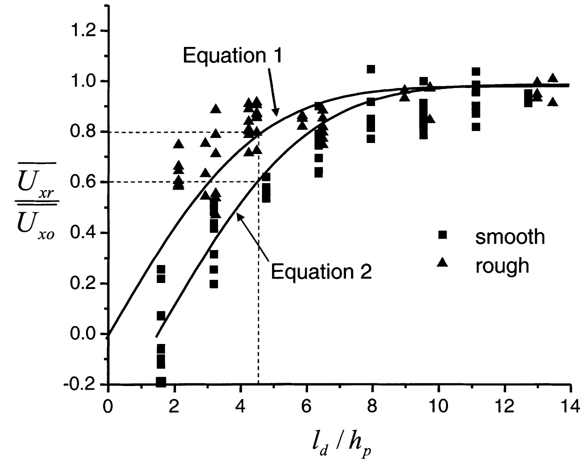

Fig. 3. Graph of $\overline{U_{xr}}/\overline{U_{xo}}$ vs. l_d/h_p for the roughened and smooth cases.

Roberson & Chen (1970) made similar measurements for the wake behind spheres and cubes resting on a smooth bed. For example, at the ratio of $l_d/D = 4{\cdot}5$ (the ratio of downstream distance to sphere diameter), Roberson & Chen (1970) found the ratio of the average velocity in the wake to that with the wake particle removed, $\overline{U_{xr}}/\overline{U_{xo}}$, to be 0·95 and 0·80 for spheres and cubes respectively. Interpolation of this ratio from the data shown in Fig. 2 is $\overline{U_{xr}}/\overline{U_{xo}} \approx 0{\cdot}7$ at $l_d/D = 4{\cdot}5$. However, the wake spheres in these experiments were not fully exposed to the flow, as they were in the Roberson & Chen (1970) experiments, and therefore a more appropriate comparison with the Roberson & Chen (1970) data set is given by l_d/h_p, where h_p is the height of the protrusion of the wake particle above that of the top of the bed particles. For the 'smooth'-bed experiments reported here, when $l_d/h_p = 4{\cdot}5$, the velocity ratio $\overline{U_{xr}}/\overline{U_{xo}} \approx 0{\cdot}6$ (Fig. 3), whereas Roberson & Chen (1970) reported a considerably larger ratio of 0·95.

Figure 3 plots $\overline{U_{xr}}/\overline{U_{xo}}$ vs. l_d/h_p for the 'smooth'- and rough-bed experiments and shows that the rough- and smooth-bed cases diverge considerably, especially at low values of l_d/h_p. Roberson & Chen (1970) stated that the wake velocity is sensitive to the turbulence intensity of the approach flow and examined the effect of a single particle on an otherwise flat bed, but they did not give values of the turbulence intensity in their experiments. The average value of the standard deviation of the downstream velocity of the approach flow in the present experiments is only 12% of the mean approach velocity in the smooth-bed experiments, whereas in the rough-bed experiments, the standard deviation is 27% of the mean. For the rough-bed experiments reported here, which have higher levels of turbulence than the smooth-bed experiments, when $l_d/h_p = 4{\cdot}5$, the velocity ratio $\overline{U_{xr}}/\overline{U_{xo}} \approx 0{\cdot}8$ (Fig. 3), which is much closer to the ratio reported by Roberson & Chen (1970) of $\overline{U_{xr}}/\overline{U_{xo}} \approx 0{\cdot}95$.

The error function is well suited to describe the data in Fig. 3 because it rises steeply from 0 and asymptotically reaches a value of 1. Hence, for the smooth-bed case, the following empirical equation is proposed to describe the velocity reduction in the wake of a protruding particle:

$$\overline{U_{xr}}/\overline{U_{xo}} = \mathrm{erf}\left(\frac{l_d - 1.5h_p}{5h_p}\right) \qquad (1)$$

and the roughened bed is empirically fit with the following equation:

$$\overline{U_{xr}}/\overline{U_{xo}} = \mathrm{erf}\left(\frac{l_d - h_p}{5h_p}\right) \qquad (2)$$

This function can then be used to describe the reduced mean downstream velocity on a particle in a natural sediment bed.

Once the mean reduction in velocity in the wakes of protrusive particles has been described empirically, a characterization of the variability of the wake velocity is needed. The ratio, $(\overline{U'^2_x})^{\frac{1}{2}}/\overline{u_x}$, of the standard deviation of the downstream velocity in the wake to the mean velocity at the same horizontal position in the wake but at a vertical position of between 0·005 and 0·014 m above the wake particle above is given in Fig. 4A vs. l_d/h_p. There is no downstream structure in the downstream velocity fluctuations (Fig. 4A), and the ratio of the standard deviation of velocity within the wake to the average velocity above the wake deviates little from the mean value of 0·26. The ratio of the standard deviation of the velocity above the wake to the mean velocity above the wake vs. l_d/h_p (Fig. 4B) again shows that there is little deviation from the mean of 0·29. Therefore, the magnitude of downstream velocity fluctuations in the wake is nearly the same as that above the wake. This result means that, even though a protruding bed particle may substantially reduce the mean velocity incident on downstream particles, the velocity fluctuations are only slightly reduced. However, the frequency structure of the velocity time series above and below the wake may be different. Unfortunately, most of the data are not sufficient to conduct a detailed time series analysis, because they were sampled unevenly in time at a rate often insufficient to resolve the turbulent fluctuations in time. Also, the data above and below the wake were collected at different times making a correlation analysis impossible.

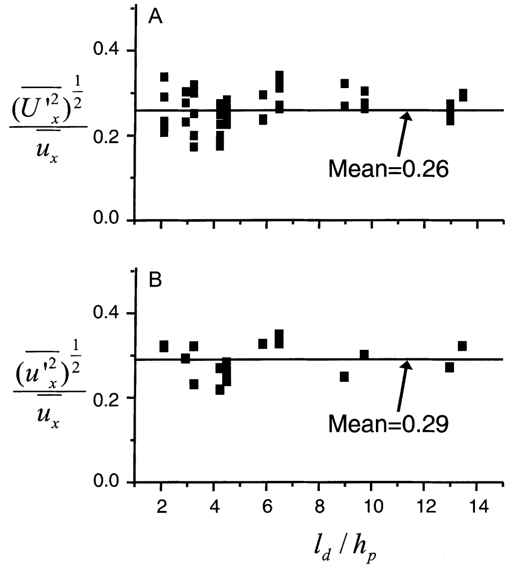

Fig. 4. Graph of relative downstream distance, l_d/h_p, vs. (A) ratio of standard deviation of velocity below the wake to mean velocity above the wake, $(\overline{U'^2_x})^{1/2}/\overline{u_x}$; (B) ratio of standard deviation to mean velocity above the wake, $(\overline{u'^2_x})^{1/2}/\overline{u_x}$.

The simplest assumption to use, given that the magnitude of the velocity fluctuations is nearly equal to that above any protruding particles, is that the velocity at a point downstream of a protruding particle is given by the mean velocity reduction in Eq. 2 plus the instantaneous deviation of the downstream velocity at the vertical position that is just above any upstream, protruding particles:

$$U_{xr} = (\overline{u}_x erf(\frac{l_d}{5h_p}) + u'_x)(1 - \frac{V_{xw}}{u_x}) \qquad (3)$$

where U_{xr} is the reduced downstream velocity including the mean and fluctuating components, and V_{xw} is the component of the velocity of the wake particle in the downstream direction. The ratio V_{xw}/u_x must be subtracted because, if the wake particle is moving close to that of the fluid, there will be little reduction in the velocity downstream of the particle.

To calculate an area-weighted reduced velocity over the face of a bed particle, U_r, the reduced velocity is averaged over the exposed area of the grain:

$$U_r = \left(\frac{1}{A_\perp}\int U_{xr}^2 dA\right)^{1/2} \qquad (4)$$

where A is the cross-sectional area of the particle perpendicular to the downstream direction. The area weighting is important because the top of the sphere has the highest incident velocity but very little area perpendicular to the flow.

MODEL OF BEDLOAD SEDIMENT TRANSPORT

An accurate model of bedload transport must incorporate the stochastic nature of the particle pocket angles, the overlying turbulence and the local modification of the turbulent field by protruding grains. A statistical mechanical approach would attempt to obtain, by either measurement and/or hypothesis, the form and interdependence of these distributions, along with a dependent distribution of saltation trajectories to close the problem. Here, rather than supply these distributions from experiments, the equations of motion of all the particles comprising a simulated bed are integrated through time while simultaneously keeping track of the interparticle interactions of all the particles. Therefore, the bed geometry is obtained through specification of the appropriate mechanics and recording of the interparticle geometries rather than by direct observation. Additionally, the grain trajectories are all calculated directly. This approach has the advantage that the pocket geometries are those produced by the imposed flow during transport, whereas direct measurements of pocket geometries are generally made at low or non-existent flow conditions when there is no transport. Also, using this discrete particle method, the local modification of the velocity field by upstream grains can be calculated using the empirical relation developed in the previous section by looking for particles that may protrude upstream of each grain. In this sense, the velocity is always locally defined and dynamic, depending on the local bed configuration at the time of calculation.

However, this method has the disadvantage that all the complexities of a natural bed, such as particle shape, cannot easily be incorporated into the model. In this model, mixed grain sizes are considered, but the shapes of the particles are taken as spheres. Although more complicated shapes such as ellipsoids may reproduce the behaviour of natural sediment better, spheres were chosen because they greatly simplify the calculations.

Equations of motion

The equations of motion provide the basis for calculation of each particle trajectory in the model. The equations of motion of a rigid particle in a viscous flow with a large Reynolds particle number can be given as:

$$(m + C_m m_f)\frac{d\vec{V}}{dt} - m_f(1 + C_m)\frac{D\vec{U}}{Dt} = (m_f - m)\vec{g} + \vec{F}_D + \vec{F}_L \qquad (5)$$

where m is the particle mass, m_f is the volume of the particle times the fluid density, $\vec{V}$ is the velocity of the particle centre of mass, $\vec{U}$ is the velocity of the fluid at the particle centre of mass if the particle was not present, C_m is the added mass coefficient (equal to 0·5 for spheres; Auton, 1987), $\vec{g}$ is gravitational acceleration, and $\vec{F}_D$ and $\vec{F}_L$ are drag and lift forces. D/Dt is the total derivative following a fluid element, and d/dt is the total derivative following the centre of the particle. Auton (1987) and Maxey & Riley (1983) have pointed out that this distinction has been missing from the analyses of particle motion presented in numerous fluid mechanics texts and papers. Unfortunately, this is also true of the previous sediment transport literature with the notable exceptions of Madsen (1991) and Niño & Garcia (1994). This confusion can result in substantial errors, because particles move from areas of low to high fluid velocity during initiation of motion, thus making the term dU/dt quite high. However, in reality, the DU/DT term is the result of turbulent pressure gradient fluctuations in the flow and is independent of the motion of a particle.

Equation 5 is similar to previously derived high particle Reynolds number equations for saltation calculations (Wiberg & Smith, 1985). For low particle Reynolds numbers, detailed solutions for the flow around a sphere have been derived that include terms such as the Stokes drag and Bassett integral history term (Maxey & Riley, 1983; Mei *et al.*, 1991). However, these solutions cannot be applied to high Reynolds flow around a particle. Additionally, potential flow solutions are inadequate to calculate the drag and lift terms. Thus, it is assumed here that the pressure distribution on the particle resulting from flow around the particle can be accounted for by a sufficient parameterization of the drag and lift terms.

The DU/DT term is difficult to estimate because it is the result of turbulent pressure fluctuations. Schmeeckle (1998) directly measured the velocity close to a stationary particle and the force on the particle synchronously and at high frequency. In this manner, the force in the downstream direction was calculated using a simple drag closure, neglecting the DU/DT term, which could then be compared with the direct force measurement. It was found that the drag closure overpredicted the downstream force by a maximum of 30% when the downstream velocity was above the mean, and substantially underpredicted the drag when the velocity was less than the mean. At the low sediment transport stages for which this model is intended, it is expected that a majority of the transport occurs when the near-bed downstream velocity is higher than the mean. Therefore, omission of the pressure fluctuation term should not result in substantial errors but, clearly, further investigation of the importance of this term is warranted.

The force measurements described above reveal that the mean vertical force on spheres in a gravel bed is much smaller than the downstream force. The force measurements also show that naturally shaped particles, however, often exhibit significant positive or negative mean vertical forces. Direct measurements of vertical forces on particles in a turbulent boundary (Willetts &

Murray, 1981; Apperley & Raudkivi, 1989; Schmeeckle, 1998) give very different vertical profile structures than often used lift force equations based on mean shear. In summary, the understanding of lift on natural particles in a sediment bed remains very poor. In the model calculations presented here, the lift force is set to zero, but the term is retained in the equations to extend the model more easily when there is a more complete understanding of lift.

Given these simplifying assumptions, when the particle whose motion is being calculated is not touching any other particles (i.e. it is saltating), the equations can be written in Cartesian co-ordinates without modification as:

$$(\rho_s + \rho_f C_m)\frac{d^2 x_i}{dt^2} = \frac{F_{Dx}}{\Gamma} - (\rho_s - \rho_f)g_x \qquad (6)$$

$$(\rho_s + \rho_f C_m)\frac{d^2 y_i}{dt^2} = \frac{F_{Dy}}{\Gamma} - (\rho_s - \rho_f)g_y \qquad (7)$$

$$(\rho_s + \rho_f C_m)\frac{d^2 z_i}{dt^2} = \frac{F_{Dz} + F_{Lz}}{\Gamma} - (\rho_s - \rho_f)g_z \qquad (8)$$

When the particle whose trajectory is being calculated is in contact with one or two other particles, it must slide and/or roll over the other particle(s). Although complicated expressions can be derived including both sliding and rolling for the initial motion of a particle, only rolling will be considered here because there is a lack of experimental and theoretical work on the dynamic sliding process between natural grains. When the centre of mass of a rolling grain is accelerated, angular acceleration of the grain about its centre of mass must also occur if no slip is to occur at the point of contact. The tangential force, $F_{\tan}$, that must be applied in order to provide angular acceleration about the centre of mass of a particle is:

$$F_{\tan} = \frac{I}{l}\frac{d^2\varphi}{dt^2} \qquad (9)$$

where I is the moment of inertia about the centre of mass, l is the moment arm, and $\partial\varphi/\partial t$ is the angular velocity about the centre of mass. For a sphere rotating about an axis through its own centre, $l = r$ and $I = 2/5mr^2$:

$$F_{\tan} = \frac{2}{5}mr\frac{d^2\varphi}{dt^2} \qquad (10)$$

When a sphere is rolling over a circle of radius r_c without slip between the surface of the sphere and the circle, the relationship between $\partial\varphi/\partial t$ and the angular velocity of the centre of mass of the sphere about the centre of the circle, $\frac{\partial\Omega}{\partial t}$ is:

$$\frac{d\varphi}{dt} = \frac{r + r_c}{r}\frac{d\Omega}{dt} \qquad (11)$$

and $F_{\tan}$ becomes:

$$F_{\tan} = \frac{2}{5}m(r + r_c)\frac{d^2\Omega}{dt^2} \qquad (12)$$

The right hand side of Eq. 12 must therefore be added to the acceleration of the centre of mass in the equations of motion.

Equations for contact with one particle

Spheres have the simplifying property that a normal to their surfaces goes through the centre mass. Therefore, the instantaneous path of the point of contact made by each sphere on the other defines part of a great circle passing through the centre of each sphere. Because of this, Eq. 12 applies to the situation at hand where r is equivalent to the radius r_i of the sphere whose equation of motion is to be integrated, and r_c is equivalent to the radius r_1 of the stationary sphere. It is convenient to write the equations of motion in spherical co-ordinates $(\varrho, \vartheta, \phi)$, where ϱ is the distance from the origin of the point of interest, ϑ is the angle between the z-axis and the line segment from the origin to the point of interest, and ϕ is the angle from the xz-plane and the plane formed by the z-axis and the point of interest. The origin of the spherical co-ordinate system is always at the centre of mass of the stationary particle $(x_1,\ y_1,\ z_1)$. Equation 12 is broken into the ϑ and ϕ directions:

$$(F_{\tan})_\vartheta = (r_i + r_1)\frac{2}{5}m\frac{d^2\vartheta}{dt^2} \qquad (13)$$

$$(F_{\tan})_\phi = (r_i + r_1)\frac{2}{5}m\frac{d^2\phi}{dt^2} \qquad (14)$$

The direction of the angular momentum vector of the moving sphere can change because its path is not restricted to that of a single circle. So, strictly, the full angular momentum equations should be solved but are neglected here. With this assumption, the equations of motion are written:

$$(r_i + r_1)\left(\frac{7}{5}\rho_s + \rho_f C_m\right)\frac{d^2\vartheta}{dt^2} + (r_i + r_1)(\rho_s + \rho_f C_m)$$
$$\sin\vartheta\cos\vartheta\left(\frac{d\phi}{dt}\right)^2 = \frac{F_{D\vartheta}}{\Gamma} + \frac{F_{L\vartheta}}{\Gamma} - (\rho_s - \rho_f)g_\vartheta \qquad (15)$$

$$(r_i+r_1)\left(\frac{7}{5}\rho_s+\rho_f C_m\right)\frac{d^2\phi}{dt^2}+2(r_i+r_1)\times(\rho_s+\rho_f C_m)\cos\vartheta\frac{d\vartheta}{dt}\frac{d\phi}{dt}=\frac{F_{D\phi}}{\Gamma}-(\rho_s-\rho_f)g_\phi \tag{16}$$

$$(r_i+r_1)(\rho_s+\rho_f C_m)\left[\left(\frac{d\vartheta}{dt}\right)^2+\left(\frac{d\phi}{dt}\right)^2\sin^2\vartheta\right]+\frac{F_{N\varrho}}{\Gamma}=\frac{F_{D\varrho}}{\Gamma}+\frac{F_{L\varrho}}{\Gamma}-(\rho_s-\rho_f)g_\varrho \tag{17}$$

where Γ is the volume of the particle, and $F_{N\varrho}$ is the normal force in the direction of ϱ that the stationary sphere exerts on the sphere in motion.

The drag, lift and gravitational forces are computed in the Cartesian co-ordinate system and are converted to spherical co-ordinates by the following equations:

$$F_\vartheta=F_x\cos\vartheta\cos\phi+F_y\cos\vartheta\sin\phi-F_z\sin\vartheta \tag{18}$$

$$F_\phi=F_x\cos\phi-F_y\sin\phi-F\sin\vartheta \tag{19}$$

$$F_\varrho=F_x\sin\vartheta\cos\phi+F_y\sin\vartheta\cos\phi+F_z\cos\vartheta \tag{20}$$

As the spherical co-ordinate system is locally defined at the origin of the stationary particle, it is necessary to convert the position of the particle back to the global Cartesian co-ordinate system using the following equations:

$$x_i=x_1+(r_i+r_1)\sin\vartheta\cos\phi \tag{21}$$

$$y_i=y_1+(r_i+r_1)\sin\vartheta\sin\phi \tag{22}$$

$$z_i=z_1+(r_i+r_1)\cos\vartheta \tag{23}$$

Equations for contact with two particles

The rotation of the centre of mass of a sphere about two fixed spheres defines a circle. Thus, it is convenient to write the equations of motion in polar co-ordinates with ξ being the distance from the origin and θ being the polar angle (Fig. 5). In this co-ordinate system, and with the distance between the origin and the centre of mass of the moving particle given as r_p, Eq. 12 becomes:

$$F_{\tan}=\frac{2}{5}mr_p\frac{d^2\theta}{dt^2} \tag{24}$$

Conversion of the equations of motion into polar co-ordinates gives:

$$r_p\left(\frac{7}{5}\rho_s+\rho_f C_m\right)\frac{d^2\theta}{dt^2}=\frac{F_{D\theta}+F_{L\theta}}{\Gamma}-(\rho_s-\rho_f)g_\theta \tag{25}$$

$$r_p(\rho_s+\rho_f C_m)\left(\frac{d\theta}{dt}\right)^2+\frac{F_{N\xi}}{\Gamma}=\frac{F_{D\xi}+F_{L\xi}}{\Gamma}-(\rho_s-\rho_f)g_\xi \tag{26}$$

where, as before, $F_{N\xi}$ represents the outward normal force exerted by the stationary spheres on the moving sphere.

The stationary spheres are assigned the subscripts 1 and 2, whereas the sphere of interest whose motion is being calculated is given the subscript *i*. It is useful to make the following definitions of the distances between the particles.

$$d_{i1}=r_i+r_1 \tag{27}$$

$$d_{i2}=r_i+r_2 \tag{28}$$

$$d_{12}=\left[(x_1-x_2)^2+(y_1-y_2)^2+(z_1-z_2)^2\right]^{1/2} \tag{29}$$

Then the angle, ζ, between the line segments extending from the centre of sphere 1 to spheres 2 and *i* is given by:

$$\zeta=\arccos\left(\frac{d_{i1}^2+d_{12}^2+d_{i2}^2}{2d_{i1}d_{12}}\right) \tag{30}$$

With this angle defined, the distance between the origin of the polar co-ordinate system and the centre of the sphere in motion is:

$$r_p=d_{i1}\sin\zeta \tag{31}$$

and the origin of the co-ordinate system in the global Cartesian co-ordinate system is:

$$x_o=x_1+(x_2-x_1)\left(1+\frac{d_{i1}^2}{d_{12}^2}-\frac{d_{i2}^2}{d_{12}^2}\right) \tag{32}$$

$$y_o=y_1+(y_2-y_1)\left(1+\frac{d_{i1}^2}{d_{12}^2}-\frac{d_{i2}^2}{d_{12}^2}\right) \tag{33}$$

$$z_o=z_1+(z_2-z_1)\left(1+\frac{d_{i1}^2}{d_{12}^2}-\frac{d_{i2}^2}{d_{12}^2}\right) \tag{34}$$

As the origin of the cylindrical co-ordinate system is always locally defined along the line segment between the two stationary particles, it is necessary to convert the new co-ordinates of

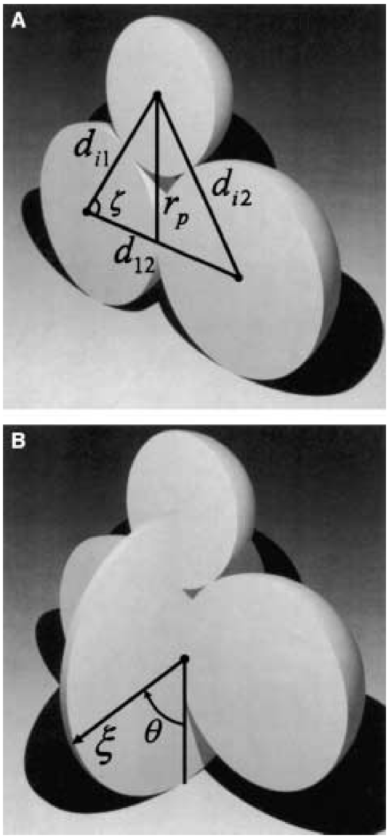

Fig. 5. Sketches showing the polar co-ordinate system formed by three spheres. (A) Distances and angle of Eqs 27–30. (B) The disc-shaped object depicts the plane of the polar co-ordinate system, and the two co-ordinate directions ξ and θ are shown on the disc.

the moving sphere back to the global Cartesian co-ordinate system at the end of each integration step. The position and orientation of the polar co-ordinate system is arbitrary relative to the global Cartesian co-ordinate system. The transformation from polar co-ordinates to the global co-ordinate system involves the conversion from polar co-ordinates to a local Cartesian co-ordinate system, and then rotation and translation of this local Cartesian system to the global co-ordinates. The *x*–*y* plane of the local Cartesian co-ordinate system, x_l, y_l, z_l, is chosen to coincide with the polar co-ordinate system so that:

$$x_l = \xi \cos\theta \tag{35}$$

$$y_l = \xi \sin\theta \tag{36}$$

$$z_l = 0 \tag{37}$$

Translation and rotation of the local Cartesian co-ordinates is accomplished by:

$$x = x_l(\hat{x}_l \cdot \hat{x}) + y_l(\hat{y}_l \cdot \hat{x}) + x_o \tag{38}$$

$$y = x_l(\hat{x}_l \cdot \hat{y}) + y_l(\hat{y}_l \cdot \hat{y}) + y_o \tag{39}$$

$$z = x_l(\hat{x}_l \cdot \hat{z}) + y_l(\hat{y}_l \cdot \hat{z}) + z_o \tag{40}$$

where the hatted characters represent unit vectors of the respective co-ordinate systems.

Carrying out this co-ordinate system transformation for the centre of mass of the moving particle gives:

$$\begin{aligned} x_i = x_o + (x_i - x_o)\cos\theta + \frac{\sin\theta}{d_{12}}((y_2 - y_1) \\ (z_i - z_o) - (z_2 - z_1)(y_i - y_o)) \end{aligned} \tag{41}$$

$$\begin{aligned} y_i = y_o + (y_i - y_o)\cos\theta + \frac{\sin\theta}{d_{12}}((z_2 - z_1) \\ (x_i - x_o) - (x_2 - x_1)(z_i - z_o)) \end{aligned} \tag{42}$$

$$\begin{aligned} z_i = z_o + (z_i - z_o)\cos\theta + \frac{\sin\theta}{d_{12}}((x_2 - x_1) \\ (y_i - y_o) - (y_2 - y_1)(x_i - x_o)) \end{aligned} \tag{43}$$

The forces that are originally calculated in the global Cartesian co-ordinates are converted to the polar co-ordinate system with:

$$\begin{aligned} F_\theta = \frac{1}{r_p d_{12}}([y_2 - y_1)(z_i - z_o) - (z_2 - z_1)(y_i - y_o)]F_x \\ + [(z_2 - z_1)(x_i - x_o) - (x_2 - x_1)(z_i - z_o)]F_y \\ + [(x_2 - x_1)(y_i - Y_o) - (y_2 - y_1)(x_i - x_o)]F_z) \end{aligned} \tag{44}$$

Algorithm

In the previous section, the equations of motion for each individual particle making up a sediment bed were specified for situations in which a particle is moving and in contact with zero, one or two other particles. In order to integrate the motion of a single particle through time, it is then necessary to decide the number of particles that the particle of interest is in contact with. Owing to the variability of fluid forces, the changing geometry of the bed and the changing location of the particle, a moving particle may lose contact with one particle or two particles simultaneously. Additionally, a particle initially at rest in contact with a number of particles may experience sufficient driving forces to initiate motion in contact with zero, one or two other particles. Conversely, a moving particle can also collide with other particles, possibly resulting in motion in contact with that particle or, if it was previously in contact with two other particles, it may come to rest on three particles. This section describes an algorithm that simultaneously integrates the equations of motion and makes all the decisions about the number of contacting particles and the results of particle collisions for all particles composing a simulated three-dimensional mixed grain-size bed. Figure 6 is a flow chart of the overall procedure of the algorithm for a single particle over a time step, Δt.

Each particle in the bed is assigned an index number, and an array is assigned to each particle that contains the index number of every particle it is in contact with. The simulation proceeds in time in small constant time steps, Δt. Starting from the first particle index number, the current state of the particle is checked (i.e. is the particle moving and, if so, in contact with how many particles?). If the particle is moving, the appropriate equation of motion is numerically integrated over Δt using the fourth-order Runge–Kutta method. Using this new position and momentum, the algorithm checks to see whether or not the particle has collided with another particle or if the particle has lost contact with one or more contacting particles. If a particle loses contact with other particles, its new state is recorded, and the contacting particle array and those of the particles that it loses contact with are adjusted accordingly. If it collides with a particle, a new momentum is calculated for the moving particle, and the position is adjusted so that the particles are just in contact; a possible new state after collision is also determined. After this, the next particle index numbers go through the same process in order until the new position, momentum and state of every particle in the bed is calculated over time Δt.

The five possible states are: (1) moving in contact with no particles; (2) moving in contact with one particle; (3) moving in contact with two particles; (4) at rest with the possibility of motion; and (5) at rest without the possibility of motion. A particle that is in contact with more than three particles has the possibility of being unable to move without one or more of the contacting particles also moving. This determination is made by calculating the equation for a plane running through each triplet of contacting points and checking to see whether any of the remaining contact points are on the other side of the plane running through the centre of particle and parallel to the triplet-defined plane. If so, then the sphere cannot move.

Collisions and initiation and cessation of motion

To check for collisions, after the integration over Δt of a particle's motion, the distance between the centre of the particle and every other particle in the bed is calculated. If the distance from the centre of the particle to that of another particle is less than the addition of the spheres' radii, then the surfaces of the particles are overlapping. As this cannot happen, a time step smaller than Δt is found using the bisection method, in which the spheres are touching within a very small tolerance limit. The particles have thus collided. If the particle whose motion is being calculated runs into a moving particle, the momentum, position and state of the particle is returned to that at the start of the integration. In other words, a moving particle is not allowed to collide with another moving particle. This introduces little error at low concentrations of moving particles and short simulation times but, at higher transport rates and long simulation times, pairs of particles will move into positions in which they collide with one another after each time step and become unable to move. Thus, the simulations presented here are for relatively short time durations and transport stages to ensure that this shortcoming of the model does not affect its results. Future development of the model will seek to allow for particles moving in contact with moving particles.

When a saltating particle contacts a bed particle, the result may be either a partially elastic rebound or viscous damping by the water that must be expelled from the gap between the two particles. Schmeeckle *et al.* (2001) have shown that the appropriate physical scaling of this problem is a collision Stokes number:

$$St = \frac{mV_{\varrho}}{6\pi\mu r_*^2} \tag{45}$$

which is a measure of the inertia of the particle relative to the viscous pressure force exerted on the particle by the fluid. Where r_* is the relative particle radius, $1/r_* \equiv 1/r_i + 1/r_1$. Schmeeckle *et al.* (2001) experimentally determined a critical particle Stokes number for natural sediment of approximately 105, below which collisions are completely viscously damped.

If a saltating particle collides with a particle at rest, the Stokes number of the collision is calculated from Eq. 45, where the velocity in the Stokes number calculation, V_{ϱ}, is the component

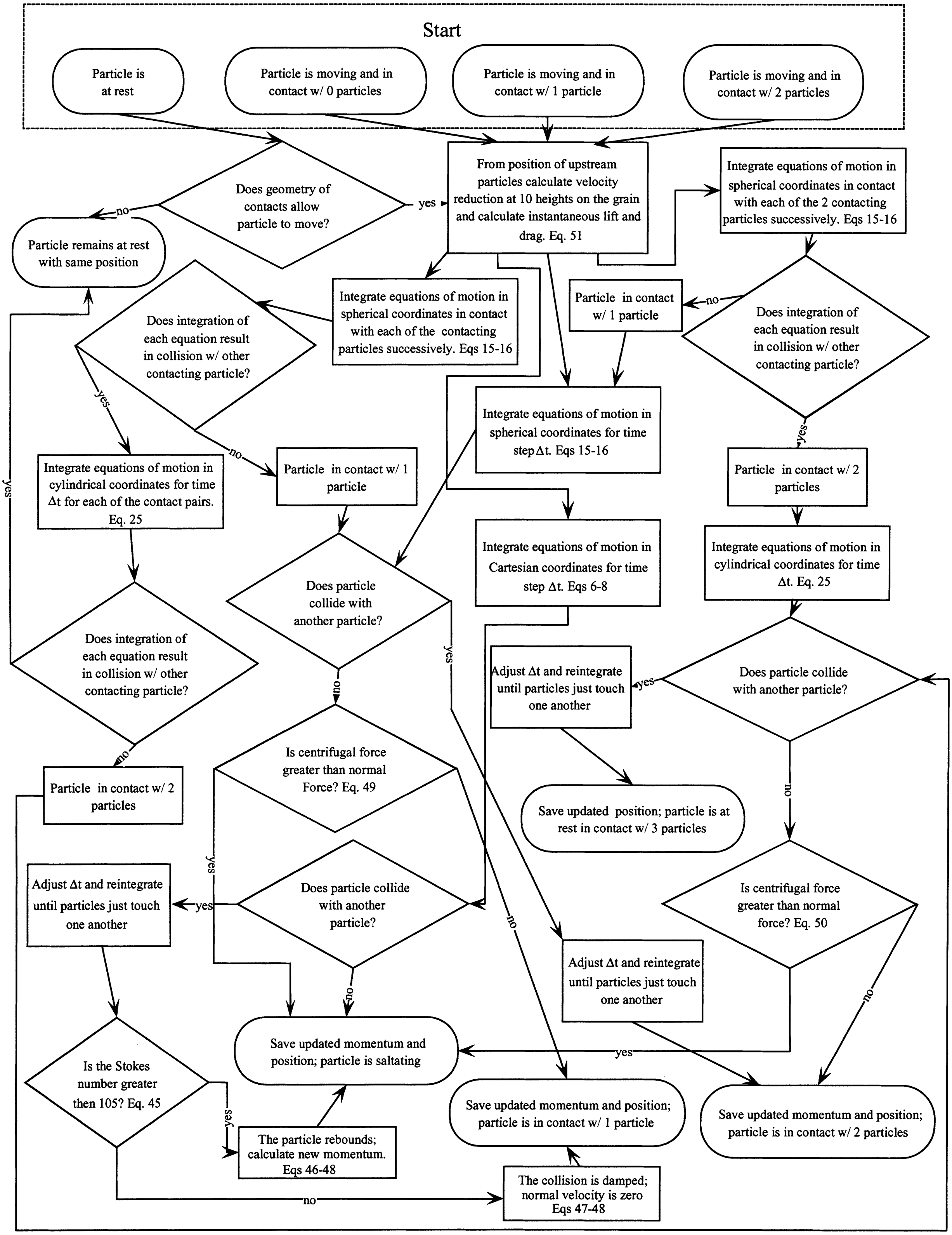

Fig. 6. Flow chart of algorithm for sediment transport simulations for a single time step and a single particle.

along the line from the centre of the moving sphere through the centre of the stationary sphere. If the Stokes number is greater than the critical value of 105, the particle rebounds, and the new velocity is calculated in spherical co-ordinates as:

$$(V_\varrho)_{\text{new}} = -e(V_\varrho)_{\text{old}} \tag{46}$$

$$(V_\vartheta)_{\text{new}} = (V_\vartheta)_{\text{old}} \tag{47}$$

$$(V_\phi)_{\text{new}} = (V_\phi)_{\text{old}} \tag{48}$$

If the Stokes number is less than 105, the tangentially directed velocities, V_ϑ and V_ϕ, are calculated with the same equations, but V is set to zero. It would be more realistic to regard e as a probability density function because of the irregular shape of natural grains, but here e is set to the experimentally determined value of 0·65, which is valid for glass spheres (Schmeeckle *et al.*, 2001).

In the event that a particle moving in contact with one particle collides with another particle, the collision is assumed to be damped, and the resultant tangential velocities are calculated as above. To determine whether the moving particle stays in contact with the previously contacted particle, a very small integration in time is performed with the particle in motion only in contact with the sphere that it has collided with. If the result of the integration is that the particle does not collide with the previously contacting particle, then it is assumed that the particle in motion is solely in contact with the newly contacted particle, and if it does recollide with the previously contacted particle, then it is assumed that the particle in motion is now moving in contact with two particles. The procedure is similar for the case in which a particle moving in contact with two particles contacts a third particle. Integration over a time step is performed in contact with the new particle, and if the particle in motion does not recontact the previously contacting particles, then the particle in motion is now moving in contact solely with the newly contacted particle. If the particle in motion recontacts one of the previously contacting particles, then integration over a time step is performed in contact with those two particles, and if it hits the third particle after this integration, then the particle is assumed to have come to rest in contact with the three particles.

At every time step, all particles that are not in motion, but whose surrounding geometry allows for the possibility of motion, are checked to see whether motion is initiated. This is accomplished by integrating the equations of motion over a small time step in contact with each individual particle and each pair of particles. If, in one of these integrations, the resultant motion does not produce a recollision with any of the other particles, then the motion of the particle is assumed to have been initiated, and its motion is calculated over Δt.

Initiation of saltation

When a particle is moving in contact with one or two particles, there is the possibility that the forces keeping it in contact will become smaller than the forces directed away from the particles that it is in contact with. Mathematically stated, the moving particle loses contact when $F_{N\varrho}$ or $F_{N\xi}$ becomes negative. The equations of motion in the radial direction can thus be manipulated to say that a particle loses contact with a single particle when:

$$(r_i + r_1)(\rho_s + \rho_f C_m)\left[\left(\frac{d\vartheta}{dt}\right)^2 + \left(\frac{d\phi}{dt}\right)^2 \sin^2\vartheta\right] > \frac{F_{D\varrho} + F_{L\varrho}}{\Gamma} - (\rho_s - \rho_f)g_\varrho \tag{49}$$

and a moving grain loses contact with two particles when:

$$r_p(\rho_s + \rho_f C_m)\left(\frac{d\theta}{dt}\right)^2 > \frac{F_{D\xi} + F_{L\xi}}{\Gamma} - (\rho_s - \rho_f)g_\xi \tag{50}$$

Thus, a large centrifugal force from a high angular velocity can cause the particle to lose contact, or a particle may simply roll off the side of the other particle(s) when the gravitational component is no longer directed in the negative radial direction. Similarly, drag and lift can also be directed radially in certain geometries.

Velocity and drag

The velocity at the top of the spheres is provided by a time series of velocity measurements taken by a laser Doppler velocimeter, LDV, a fraction of a grain diameter above a sediment bed. The algorithm is fully capable of calculating force in response to fluctuations in vertical and cross-stream velocity but, for the simulations here, only the downstream velocity, u_x, is considered. As the measurements of velocity used to drive the model were taken at a point, a method is required to extrapolate the time series from a point horizontally across the width and length of the simulated bed. It is assumed that the instantaneous velocity is constant in the cross-stream direction. In the downstream direction, the velocity is assumed to be advected downstream at the mean velocity. So, for example, if $u_x(x, t)$ is the instantaneous downstream velocity at the upstream-most point of the bed, measured at the top of the bed, then the same velocity will occur downstream after time period, $l/\overline{u_x}$, where l is the downstream distance. Thus, $u_x(x,t) = u_x(x+l,\ l/\overline{u_x})$.

The drag on a particle is a function of the downstream velocity incident on the face of the particle. Equation 3 provides the basis for a calculation of the reduced velocity on the face of the particle for the purpose of the calculation of instantaneous drag. The calculation proceeds by breaking the sphere into 10 horizontal zones; the area of each of these zones is calculated based on the equation for a horizontal slice of a circle. Next, from a point having the x and y co-ordinates of the centre of the sphere and a z co-ordinate at the centre of the horizontal slice, a line is projected out parallel to the x-axis in the upstream direction. Any sphere within 10 mean grain diameters upstream of the centre of the particle is checked to see whether it intersects with the line. For particles that intersect with the line, the ratio of downstream distance to protrusion height above the line is calculated. The particle that has the smallest ratio is selected as that which produces the reduction in velocity on the vertical slice. The reduced velocity, U_{xr}, from Eq. 3 is used to calculate the instantaneous drag on a particle as:

$$F_{Dx} = \frac{\rho_f}{2} C_D \int (U_{xr} - V_x)^2 dA \tag{51}$$

The calculation of drag using the reduced velocity is the means by which the spatial variability in drag force is calculated. It is applied to each grain making up the bed, and each individual particle has a different drag because of the position and velocity of upstream grains. For mixed grain-size beds, smaller particles will tend to have smaller incident areas and reduced velocities than larger grains. Hence, there is no need for purely empirically based hiding functions, which are part of many mixed grain-size sediment transport equations.

Simulations

To test the model, simulations composed of two different grain-size distributions were performed. One set of simulations involved uniformly sized spheres. The diameter of the spheres was set to 0·0286 m. The second set of simulations involved a mixed grain-size distribution in which the diameters were chosen randomly from a log-normal distribution on a number basis. The mean diameter was set at 0·005 m, and the standard deviation was set to 0·002 m. For both cases, the velocity time series used was that of a time series of velocity measured very near a gravel bed. These observations were taken at a height of ≈0·007 m above the top of a gravel bed in a laboratory water flume. The gravel was well sorted and well rounded with a mean grain diameter of 0·023 m. A second measurement taken 0·001 m from the bed had the same mean velocity (0·251 m s^{-1} vs. 0·250 m s^{-1}). This observation is in keeping with other observations of the break in slope of the log velocity profile and reduction in shear very near a rough bed (Nowell & Church, 1979; Pitlick, 1992; Dittrich *et al.*, 1996). The time series at 0·07 m above the bed was used because, at this elevation (slightly less than one-third of a grain diameter), there is little chance that it was affected by upstream, protruding grains. Below the level of the tops of the grains, it is a safe assumption that vertical momentum transport is dominated by the drag on bed particles, and there is no attempt to calculate transport of momentum by Reynolds stresses within the fluid. The velocity of the measured time series is far less than required to move any grains in the simulated bed, so all the velocities are multiplied by a constant factor. The shear velocity for each simulation is obtained by multiplying the directly measured shear velocity by the same constant factor, under the assumption that the mean velocity scales with the shear velocity.

A bed of particles needs to be generated before the simulations can be conducted. This is accomplished by setting the fluid velocities to zero and then dropping spheres from a sufficient height above the bed. The equations of motion of the dropped particle are integrated until it comes to rest, whereupon the next particle is dropped from a random horizontal position above the bed. The first particles to be dropped will not encounter any other particles. So, they come to rest when the height above $z = 0$ of the centre of the sphere is equal to the radius of the sphere. Particles generated later will generally first hit a single particle then roll down in contact until a second and eventually a third particle is encountered, whereupon they come to rest. The critical Stokes number is essentially set to infinity, so that all collisions are inelastic. This speeds up the time required for a particle to come to rest, because the particles cannot rebound when they collide. The dimensions of the bed are set to a specific width and length with all boundaries periodic. The most upstream part of the bed is given an x co-ordinate of 0 and the most downstream x co-ordinate is L, whereas the y co-ordinates of the sides of the bed are 0 and W. A particle whose x co-ordinate becomes greater than L reappears at the upstream end with an x co-ordinate of the old x co-ordinate minus L, and a particle whose x co-ordinate becomes less than 0 reappears at the downstream end. The same argument holds for the sides of the simulated bed; a particle that goes out one side of the bed comes in the other. When checking to see whether a particle near an edge of the bed has collided with another particle, it is necessary to check for particles on the opposite edge, as a particle that overlaps an edge is essentially on both sides: either the upstream and downstream end or both sides. A particle overlapping a corner is present at all four corners. The mixed grain-size beds have $L = 0{\cdot}20$ m and $W = 0{\cdot}05$ m, whereas the uniform bed has $L = 0{\cdot}60$ m and $W = 0{\cdot}15$ m.

A 5 s piece of the velocity time series was used to calculate the transport in the mixed grain-size simulations, and a 20 s piece was used in the uniform size simulations. This essentially amounted to two major transport events in the 5 s simulations and five in the 20 s simulations. Longer time series result in reduced transport rates because of the build-up of particles that are in contact and trying to move simultaneously. The transport is seen to be highly episodic and correlated with the instantaneous downstream velocity; at periods of low, instantaneous, downstream velocity, the transport is generally nonexistent. This result is precisely what has been quantified by Nelson *et al.* (1995) with measured instantaneous transport rates using high-speed motion photography synchronous to high-frequency, near-bed, LDV measurements of downstream velocity. Nelson *et al.* (1995) also found that transport was not correlated with either instantaneous vertical velocity or instantaneous Reynolds stress. Figure 7 is a graph of the time series used in the mixed grain-size case along with the instantaneous volumetric transport rate, q_s. The transport rate was calculated by adding the volume of all the particles that left the downstream end of the bed in a 0·2 s interval and subtracting the volumes of the few particles that travelled upstream of the $x = 0$ co-ordinate. It can be seen that almost all the transport occurs just after the peak in the velocity fluctuation, and the peak of the transport is slightly lagged in time compared with the peak of the velocity fluctuation. This lag time in transport was also seen in the experiments of Nelson *et al.* (1995) and is apparently caused by the fact that a positive velocity fluctuation moves downstream slightly faster than the grains that it transports.

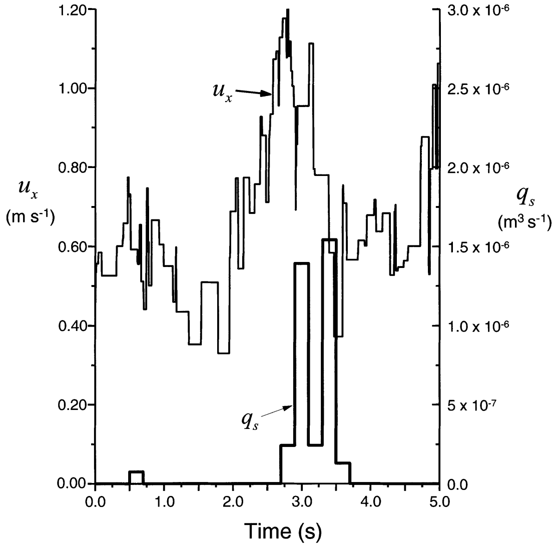

Fig. 7. Sediment flux, q_x, and downstream velocity, u_x, as a function of time for a mixed grain-size simulation.

The total transport for each of the simulations is shown in Fig. 8 in terms of the non-dimensional

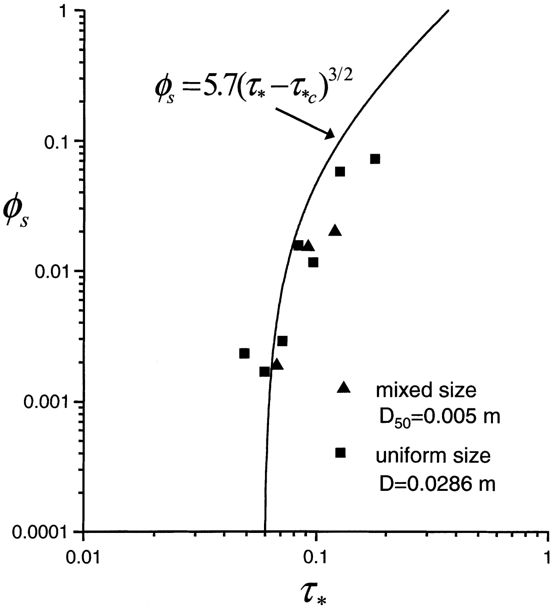

Fig. 8. Calculated non-dimensional transport rates, ϕ_s, vs. non-dimensional boundary shear stress, τ_*. An empirical bedload formula of Fernandez-Luque & van Beek (1976) is also plotted.

transport rate ϕ_s as a function of non-dimensional stress, τ_*. The non-dimensional transport rate and stress are defined by:

$$\phi_s = \frac{q_s}{[(\rho_s/\rho_f - 1)gD^3]^{1/2}} \tag{52}$$

$$\tau_* = \frac{\tau_b}{(\rho_s - \rho_f)gD} \tag{53}$$

with D_{50} being used for the mixed-size case. The empirical bedload equation of Fernandez-Luque & van Beek (1976) is also shown in Fig. 8 with $\tau_{*c} = 0{\cdot}06$.

For the mixed grain-size simulation with the highest transport shown in Fig. 8, the position of each of the particles after every 0·01 s was recorded to memory. Each of these time slices was turned into ray-traced images such as Fig. 9, and all the images were strung together to make an animation of the simulation. This animation is available for download and viewing in the audio video interleave (AVI) format (see *Supplementary material*). Several interesting observations were made from this animation.

When the velocity was low, there was almost no transport; only occasionally would a particle roll out of its pocket and quickly stop in a pocket one or several diameters downstream. Also, during periods of low velocity, several grains were seen to move back and forth within their pockets. This behaviour may have been caused partly by high frequency fluctuations in force on the grains but, more often, it appeared to be caused by collisions with another grain, whereupon the angle of ascent to move forward was steeper. For idealized initial motion geometries, such as a sphere moving over another single sphere, the angle of ascent decreases with forward motion, thus precluding this type of motion.

When the instantaneous downstream velocity became high, particles were rapidly entrained by the flow and began to saltate. The saltation lengths were from several to about 10 mean grain diameters in length, and trajectory heights were generally about two grain diameters high. Some trajectory heights were about four diameters from the bed. Figure 9 is an image showing several particles at the top of their trajectories at the peak of a high transport event. High trajectories were caused by collisions with large bed grains that protruded far above the mean bed elevation.

Once the period of high instantaneous downstream velocity subsided, disentrainment occurred rapidly, although not as rapidly as the initial entrainment. A particle bounces once or twice with subsequent saltation trajectories being a grain diameter or less. Eventually, the collision between another grain is viscously damped, and rolling in contact with another particle commences. A particle then quickly comes to rest in a pocket.

One of the most notable features of this animation, which appears to be true of all the simulations from an examination of the transport time series, is the lack of a period in which there is a substantial amount of rolling. As explained before, the only rolling that took place was an occasional movement one or two grain diameters downstream. Some researchers have thought that, at transport stages just above critical, rolling was the dominant mode of transport, which then gave way to saltation as the transport stage increased.

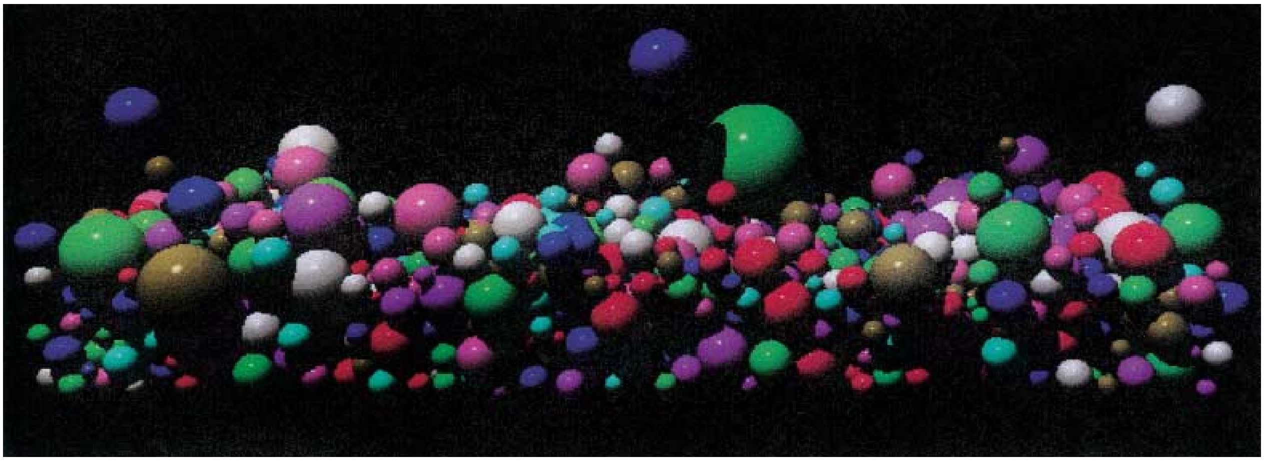

Fig. 9. Ray-traced image of simulated mixed grain-size bed during transport. The length of the bed is 0·20 m, and the upstream and downstream edges of the bed are visible at the left and right edges of the image respectively. This image is part of an animation that is available on Blackwell Publishing's *Sedimentology* website (see text for details).

These simulations suggest that the qualitatively defined critical shear stress may be the break between a near-bed flow strength that is sufficient to produce rare instances of saltation and one that is not. Marginal transport below this critical condition would be wholly composed of rare movements one or two pockets downstream.

Hiding and pocket friction angles in a mixed grain-size bed

Each individual particle in the simulations has a different drag because of the positions of upstream grains, and each grain rests upon downstream grains at differing angles to the vertical. A simulation of a relatively large mixed grain-size bed was conducted to show the distributions of pocket friction angles and hiding of particles vs. grain size. The bed is composed of spheres with a log-normal distribution of diameters. The mean diameter is 0·005 m, and the standard deviation is 0·002 m. The length and width of the simulated bed were 1·00 m and 0·10 m respectively. The bed was subjected to the 5 s velocity time series shown in Fig. 7, and then subjected to zero velocity for 2 s to ensure that all moving particles came to rest.

Smaller particles will tend to have smaller incident areas and reduced velocities than larger grains, because they are unlikely to protrude above the larger particles. To illustrate this point, the time-averaged squared reduced velocity ratio, $(\overline{U_r}/\overline{U_0})^2$, is computed for each of the topmost particles of the simulated bed and plotted vs. relative grain size in Fig. 10. This is essentially the ratio of the time-averaged drag force resulting from hiding to the time-averaged drag force if the grain were fully exposed to the flow. Thus, when $(\overline{U_r}/\overline{U_0})^2$ is near 1, the reduction in the mean drag force due to upstream, protruding grains is minimal, and when the ratio is near 0, the reduction in mean velocity is nearly complete. Figure 10 shows that the reduction in velocity for most small particles is nearly complete, whereas larger particles tend to have an equal distribution of relatively large and small incident velocities. The median and upper and lower quartiles of $(\overline{U_r}/\overline{U_0})^2$ were calculated for bins of D/D_{50} with a width of 0·5. The upper quartile is the value of $(\overline{U_r}/\overline{U_0})^2$ for which 25% of the particles in the bin are greater than, and the lower quartile is the value for which 25% are less than. The median and quartiles show a pronounced increase in the relative drag force reduction with a decrease in size. A very small percentage of small particles experiences a substantial mean drag force. Only turbulent fluctuations, as represented in Fig. 4, are available to entrain the great majority of small particles.

The distribution of pocket friction angles vs. particle size of the simulated bed was measured. For each particle at the top of the bed, the gravitational component was tilted in Eqs 15, 16 and 25 from vertical to an increasing angle in the downstream direction until the particle began to move. In essence, this is the numerical equivalent of a tilting board experiment. Figure 11 is a plot of the angle at which motion begins vs. relative grain size. Particles with high angles require more force to move than particles at low angles of the same size. The mean and median pocket friction angles for all the particles are 49° and 48°, respectively, whereas the

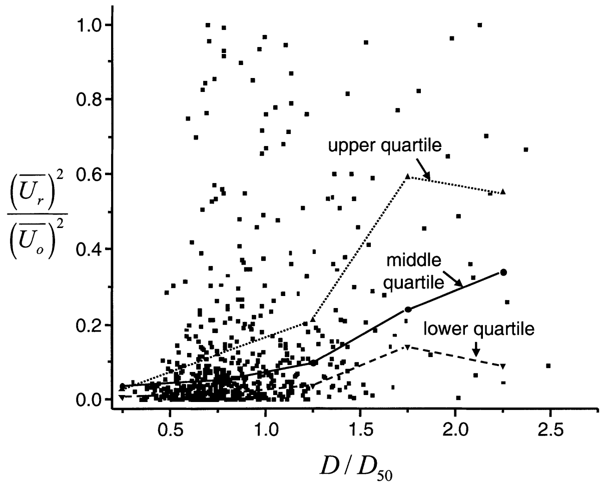

Fig. 10. Squared ratio of reduced velocity to fully exposed velocity, $(\overline{U_r}/\overline{U_0})^2$, vs. relative grain size, D/D_{50}.

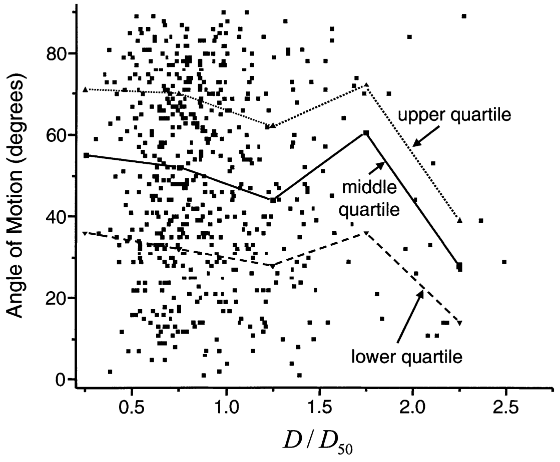

Fig. 11. Pocket friction angle vs. relative grain size, D/D_{50}.

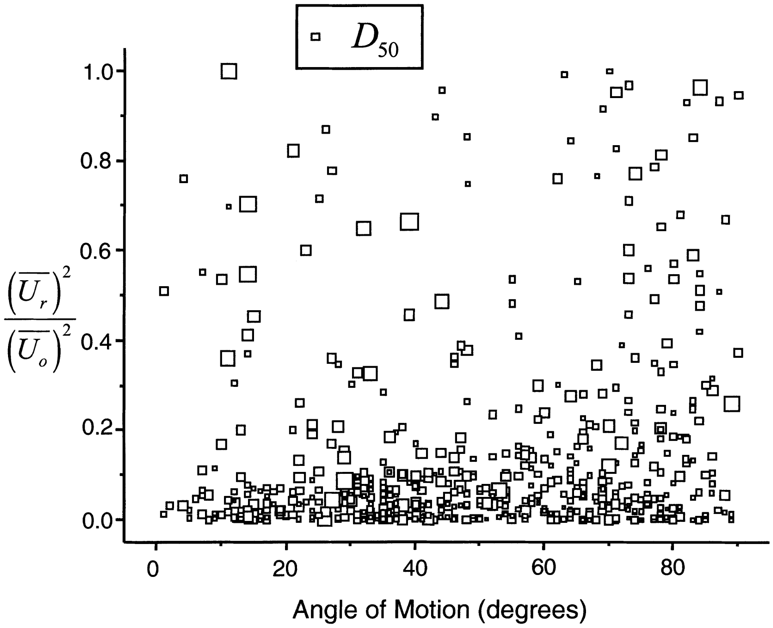

Fig. 12. Squared ratio of reduced velocity to fully exposed velocity, $(\overline{U_r}/\overline{U_0})^2$, vs. pocket friction angle. The width of each square is proportional to the particle diameter.

median and mean pocket angles of the bed before motion were 39° and 37°. The increase in mean and median pocket angles for water-worked beds has been documented in previous studies (Kirchner *et al.*, 1990; Buffington *et al.*, 1992). The median and quartiles of the pocket angles for bins of D/D_{50} with a width of 0·5 are also plotted in Fig. 11. Johnston *et al.* (1998) measured the *in situ* friction angles of five water-worked, mixed grain-size river beds. The median pocket friction angles for the particles in these beds ranged from 46° to 70°. Two of the five beds had no noticeable change in the median or quartile friction angles, whereas the other three beds showed a decrease in friction angle with an increase in grain size. Thus, the friction angles developed by the simulated bed appear to have a distribution that is similar to those of natural water-worked river beds. The simulated bed has mean friction angles that are on the low side of the range of beds measured by Johnston *et al.* (1998), which is in keeping with tilting board experiments that show lower mean friction angles for more spherical and less angular particles (Miller & Byrne, 1966).

Only a small portion of particles in the simulated bed has a significant mean downstream incident velocity. Therefore, only when the instantaneous velocity is high can any but a few of the particles move, depending also on the pocket angles in which the grains rest. Particles that have small pocket friction angles and are relatively exposed to the flow are the most easily entrained. Figure 12 shows the pocket friction angle vs. $(\overline{U_r}/\overline{U_0})^2$ for the simulated bed. The width of each square in Fig. 12 is scaled to the diameter of the particle that it represents. The particles in the upper left hand corner of Fig. 12 are the most readily moved. Few particles have small friction angles and high incident velocities. The particles that have high incident velocities and low pocket friction angles tend to be larger than the median grain size. This would have to be the case if the larger particles are to be entrained at a similar rate to the smaller particles, because the larger particles are harder to move on account of their larger mass.

Effect of magnitude of near-bed turbulent events

To illustrate the importance of high instantaneous downstream velocities on the transport rate, a series of simulations was conducted of a flow with identical mean velocity but a varying amplitude. A sinusoidal wave with a period of 0·5 s and an average near-bed velocity, $\overline{u_x}$, of 1·20 m s^{-1} over a uniform grain-size bed, $D =$ 0·0286 m. The simulations were run for 6 s, and the amplitude of the sinusoidal wave was varied from 0 to 0·9 times the average velocity. The chosen average near-bed velocity corresponds approximately to a transport stage, τ_*/τ_{*c}, of 1·5. The increase in transport with an increase in amplitude is dramatic (Fig. 13). In fact, there is no transport below an amplitude ratio of 0·2; transport only takes place because of near-bed velocities that are greater than the mean. The magnitude and duration of turbulent events that

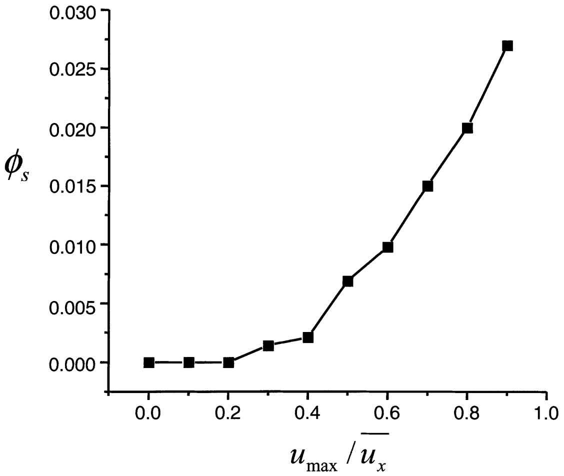

Fig. 13. Non-dimensional transport rate as a function of amplitude of near-bed velocity fluctuations.

produce high near-bed downstream velocities thus control the time-averaged transport rate.

CONCLUSIONS

The challenge to building a physical model of bedload transport is to characterize the tails of several distributions while at the same time incorporating the physical fact that the entrainment, disentrainment and motion of individual grains is the result of forces applied to each grain by the fluid. A discrete particle model, as presented here, is probably the simplest way of incorporating these two aspects of the problem. The distributions of pocket angles and protrusion heights are consequentially calculated by directly calculating the equations of motion of each particle while keeping track of interparticle interactions. Because the bedload sediment transport model is based directly on the coupling of near-bed fluid to the sediment grains, no assumption is made about the variability of the near-bed flow in relation to the shear velocity. Therefore, it is a unique model in its ability to predict sediment transport in non-uniform flows.

At low transport stages, bedload is poorly characterized by mean properties of the flow and sediment bed. Very few grains move when the near-bed velocity is at the mean. Grains resting in average pocket angles rarely move compared with particles in more favourable pocket geometries, and particles at the top of a sediment bed that protrude an average amount above a level datum are less responsible for the transport rate than more protrusive particles. Thus, it is no surprise that the Bagnold boundary condition performs poorly at low transport stages; the mean influence of moving particles on the near-bed velocity field is much less important than the magnitude and temporal extent of turbulent events that are capable of transporting sediment. At higher shear stresses, the transport of sediment by the mean near-bed velocity will be considerable, and moving grains will extract enough momentum from the flow to limit the entrainment rate.

The near-bed velocity measurements presented here were made among static bed particles. No comparable measurements of near-bed fluid velocities have been made during bedload transport, because it is difficult to measure fluid velocities at a fixed point that has bedload particles moving through it. However, measurements of velocity within the bedload layer are essential to understanding how moving particles modulate the mean and fluctuating components of the fluid velocity. The fluid velocity reduction caused by moving grains in the model presented here only affected the local area downstream of each grain. The moving grains do not reduce the velocity of the layer in a spatially averaged sense. Previous models of bedload transport took the opposite approach and only modelled the layer-averaged velocity reduction and disregarded the local velocity reduction. With the rapid advancement of particle imaging velocimetry (PIV) techniques, it may now be possible to measure velocities within the bedload layer. With knowledge of the velocity structure within the bedload layer, a complete model of bedload transport could be built that includes the importance of turbulence fluctuations in entraining grains at low to moderate transport stages, and also includes the feedback that moving grains have on the fluid velocity in the whole bedload layer, which is important for moderate to high transport stages.

ACKNOWLEDGEMENTS

Substantial improvements from an earlier manuscript resulted from the thorough and thoughtful reviews by Ian McEwan, Pat Wiberg and James Best. Much of this research was completed while the first author was employed by the United States Geological Survey's National Research Program. This work was supported by two National Science Foundation grants: EAR-950641 to Ronald L. Shreve and Jonathan M. Nelson through the University of California, Los Angeles, and EAR-012446 to Mark W. Schmeeckle through Florida State University.

SUPPLEMENTARY MATERIAL

The following material is available from: http://www.blackwellpublishing.com/products/journals/suppmat/SED/SED555/SED555sm.htm

Fig. S1. This animation is a visualization of a direct numerical simulation of mixed grain size bedload transport in response to a unidirectional, time-varying (turbulent), near-bed, downstream velocity.

NOMENCLATURE

$A_\perp$	maximum cross-sectional area of the particle in a plane perpendicular to the flow direction;
C_m	coefficient of added mass;
C_D	drag coefficient;
d_{i1}, d_{i2}, d_{i3}	distance between the centres of mass of: the moving particle and the first stationary particle; the moving particle and the second stationary particle; the two stationary particles;
D	grain diameter;
D_{50}	median grain diameter;
e	coefficient of restitution;
F_D	drag force;
F_L	lift force;
F_N	force normal to the surface of contact between two particles;
$F_{\tan}$	force tangential to the surface of contact between two particles;
g	gravitational acceleration;
h_p	height of protrusion of the wake particle above that of the bed particles;
I	moment of inertia;
l	downstream distance;
l_d	downstream distance from the centre of the wake-producing particle;
L	downstream length of the computational domain;
m	particle mass;
m_f	mass a particle would have if its density was that of the fluid;
n	number of particles in motion per unit area;
r	particle radius;
r_i, r_1, r_2	radius of the particle in motion, the first stationary particle, the second stationary particle;
r_c	radius of the particle that is stationary;
r_p	distance between the origin of the polar co-ordinate system and the centre of the moving particle;
r_*	relative particle radius, $1/r_* \equiv 1/r_i + 1/r_1$;
St	collision Stokes number;
t	time;
Δt	time step;
u_x, u_y, u_z	fluid velocity in the x, y and z directions;
$u'_x \equiv u_x - \overline{u}_x, u'_y \equiv u_y - \overline{u_y}, u'_z \equiv u_z - \overline{u_z}$	deviation from time-averaged velocity;
$u_* \equiv \sqrt{\tau_b/\rho_f}$	shear velocity;
$u_{\max}$	amplitude of variation of u_x for the simulations in which a sinusoidal variation of u_x was imposed at the top of the sediment bed;
U_{xr}	velocity in the x direction at a vertical position below that of an upstream particle that is reduced relative to the velocity that would exist if the upstream particle were to be removed;
U_r	area-weighted spatial average of U_{xr};
U_{xo}	velocity in the x direction at a vertical position below that of an upstream particle that would exist if the upstream particle were to be removed;
U_o	area-weighted spatial average of U_{xo};
V_x, V_y, V_z	particle velocity in the x, y and z directions;
V_{xw}	velocity of the wake-producing particle in the x direction;
W	cross-stream width of the computational domain;
x, y, z	global Cartesian co-ordinates;
x_l, y_l, z_l	local Cartesian co-ordinates;
$\hat{x}, \hat{y}, \hat{z}$	unit vectors in the global Cartesian co-ordinate system;
$\hat{x}_l, \hat{y}_l, \hat{z}_l$	unit vectors in the local Cartesian co-ordinate system;
x_o, y_o, z_o	position of the origin of the local co-ordinate system in global Cartesian co-ordinates;
x_i, y_i, z_i	position of the centre of mass of the moving particle in global Cartesian co-ordinates;
x_1, y_1, z_1	position of the centre of mass of the first stationary particle in global Cartesian co-ordinates;

x_2, y_2, z_2	position of the centre of mass of the second stationary particle in global Cartesian co-ordinates;
ζ	the angle between the line segments extending from the centre of sphere 1 to spheres 2 and i;
ξ, θ	polar co-ordinates;
ϱ, ϑ, ϕ	spherical co-ordinates;
$\frac{\partial\varphi}{dt}$	angular velocity of a particle about its centre of mass;
$\frac{\partial\Omega}{dt}$	angular velocity of the centre of mass of a particle about the centre of mass of another particle;
ρ_f	density of the fluid;
ρ_s	density of the sediment;
μ	dynamic viscosity of the fluid;
τ_b	boundary shear stress;
τ_c	critical shear stress;
τ_*	non-dimensional shear stress;
τ_{*c}	non-dimensional critical shear stress;
Γ	volume of the particle;
ϕ_s	non-dimensional sediment transport rate.

REFERENCES

Apperley, L.W. and **Raudkivi, A.J.** (1989) The entrainment of sediments by the turbulent flow of water. *Hydrobiologia*, **176/177**, 39–49.

Ashida, K. and **Michiue, M.** (1972) Study on hydraulic resistance and bedload transport in alluvial streams. *Proc. Jpn Soc. Civ. Eng.*, **206**, 59–69.

Auton, T.R. (1987) The lift force on a spherical body in a rotational flow. *J. Fluid Mech.*, **183**, 199–218.

Bagnold, R.A. (1956) The flow of cohesionless grains in fluids. *Trans. Roy. Soc. London A*, **249**, 235–297.

Bayazit, M. (1975) Free surface flow in a channel of large relative roughness. *J. Hydraul. Res.*, **14**, 115–126.

Buffington, J.M., Dietrich, W.E. and **Kirchner, J.W.** (1992) Friction angle measurements on a naturally formed gravel streambed: implications for critical boundary shear stress. *Water Resour. Res.*, **28**, 411–425.

Dittrich, A., Nestmann, F. and **Ergenzinger, P.** (1996) Ratio of lift and shear forces over rough surfaces. In: *Coherent Flow Structures Open Channels* (Eds P.J. Ashworth, S.J. Bennett, J.L. Best and S.J. McLelland), pp. 6:1–21. John Wiley and Sons, Chichester.

Fernandez-Luque, R. and **van Beek, R.** (1976) Erosion and transport of bed-load sediment. *J. Hydraul. Res.*, **14**, 127–144.

Gomez, B. (1993) Roughness of stable, armoured gravel beds. *Water Resour. Res.*, **29**, 3631–3642.

Grass, A.J. (1970) Initial instability of fine bed sand. *J. Hydraul. Eng.*, **96**, 619–632.

Gyr, A. and **Schmid, A.** (1997) Turbulent flows over smooth erodible sand beds in flumes. *J. Hydraul. Res.*, **35**, 525–544.

Johnston, C.E., Andrews, E.D. and **Pitlick, J.** (1998) In situ determination of particle friction angles of fluvial gravels. *Water Resour. Res.*, **34**, 2017–2030.

Kirchner, J.E., Dietrich, W.E., Iseya, F. and **Ikeda, H.** (1990) The variability of critical shear stress, friction angle, and grain protrusion in water-worked sediments. *Sedimentology*, **37**, 647–672.

Lee, H. and **Hsu, I.** (1994) Investigation of saltating particle motions. *J. Hydraul. Eng.*, **120**, 831–845.

McLean, S.R., Nelson, J.M. and **Wolfe, S.R.** (1994) Turbulence structure over two-dimensional bedforms: implications for sediment transport. *J. Geophys. Res.*, **99**, 12,729–12,712,747.

Madsen, O.S. (1991) Mechanics of cohesionless sediment transport in coastal waters. In: *Coastal Sediments '91: Proceedings* (Eds N.C. Kraus, K.J. Gingerich and D.L. Kriebel), pp. 1:15–27. American Society of Civil Engineers, Reston.

Maxey, M.R. and **Riley, J.J.** (1983) Equation of motion for a small rigid sphere in a non-uniform flow. *Phys. Fluids*, **26**, 883–889.

Mei, R., Adrian, R.J. and **Hanratty, T.J.** (1991) Particle dispersion in isotropic turbulence under Stokes drag and Basset force with gravitational settling. *J. Fluid Mech.*, **225**, 481–495.

Miller, R.L. and **Byrne, R.J.** (1966) The angle of repose for a single grain on a fixed rough bed. *Sedimentology*, **6**, 303–314.

Nelson, J.M., McLean, S.R. and **Wolfe, S.R.** (1993) Mean flow and turbulence fields over two-dimensional bed forms. *Water Resour. Res.*, **29**, 3935–3953.

Nelson, J.M., Shreve, R.L., McLean, S.R. and **Drake, T.G.** (1995) Role of near-bed turbulence structure in bed-load transport and bed form mechanics. *Water Resour. Res.*, **31**, 2071–2086.

Niño, Y. and **Garcia, M.** (1994) Gravel saltation, 2. Modeling. *Water Resour. Res.*, **30**, 1907–1914.

Niño, Y., Garcia, M. and **Ayala, L.** (1994) Gravel saltation, 1. Experiments. *Water Resour. Res.*, **30**, 1907–1914.

Nowell, A.R.M. and **Church, M.** (1979) Turbulent flow in a depth-limited boundary layer. *J. Geophys. Res.*, **84**, 4816–4824.

Owen, P.R. (1964) Saltation of uniform grains in air. *J. Fluid Mech.*, **20**, 25–242.

Pitlick, J. (1992) Flow resistance under conditions of intense gravel transport. *Water Resour. Res.*, **28**, 891–903.

van Rijn, L.C. (1984) Sediment transport, part 1: bed load transport. *J. Hydraul. Eng.*, **110**, 1431–1456.

Roberson, J.A. and **Chen, C.K.** (1970) Flow in conduits with low roughness concentration. *J. Hydraul. Eng.*, **96**, 941–957.

Robert, A. (1990) Boundary roughness in coarse-grained channels. *Prog. Phys. Geogr.*, **14**, 41–70.

Schlichting, H. (1979) *Boundary-Layer Theory*. McGraw-Hill, New York, 817 pp.

Schmeeckle, M.W. (1998) *The mechanics of bedload sediment transport*. PhD Thesis, University of Colorado, Boulder, 158 pp.

Schmeeckle, M.W., Nelson, J.M., Pitlick, J. and **Bennett, J.P.** (2001) Interparticle collision of natural sediment grains in water. *Water Resour. Res.*, **37**, 2377–2391.

Sekine, M. and **Kikkawa, H.** (1984) Transportation mechanism of bed-load in an open channel. *Proc. Jpn Soc. Civ. Eng.*, **351**, 247–250.

Sekine, M. and **Kikkawa, H.** (1992) Mechanics of saltating grains. II. *J. Hydraul. Eng.*, **118**, 536–558.

Stull, R.B. (1988) *An Introduction to Boundary Layer Meteorology*. Kluwer Academic Publishers, Dordrecht, 666 pp.

Wiberg, P.L. and **Smith, J.D.** (1985) A theoretical model for saltating grains in water. *J. Geophys. Res.*, **90,** 7341–7354.

Wiberg, P.L. and **Smith, J.D.** (1987) Initial motion of coarse sediment in streams of high gradient. In: *Erosion and Sedimentation in the Pacific Rim* (Eds R.L. Beschta, T. Blinn, G.E. Grant, G.G. Ice and F.J. Swanson), pp. 299–308. International Association of Hydrological Sciences, Wallingford.

Willetts, B.B. and **Murray, C.G.** (1981) Lift exerted on stationary spheres in turbulent flow. *J. Fluid Mech.*, **105,** 487–505.

Manuscript received 30 October 2000;
revision accepted 8 January 2003.